The Journal of Green Energy and Environmental Engineering

Research Paper

Preparation and Corrosion Inhibiting Mechanism of Bio-based Cerium Phytate Nanoparticles

Steve C. Arnold[1], Dmitry Domegan[2,*]

[1] College of Life Science, University of Central Florida, Unites States
[2] Marketing Discipline, J.E. Cairnes School of Business and Economics, National University of Ireland Galway, Galway, Ireland
*Corresponding author: Sarnold@ucf.edu; DDMARK@nuigalway.ie

Abstract. Bio-based cerium phytate (Ce-PA) was synthesized using phytic acid (PA) and cerium nitrate. Subsequently, a series of epoxy coatings with varying Ce-PA contents (based on the mass of epoxy resin) were prepared. Ce-PA was characterized by FTIR, TGA, and SEM. The microstructural characteristics, mechanical performance, and corrosion protection efficacy of the coatings were systematically assessed, and the protective mechanism of Ce-PA within the epoxy matrix was elucidated. The results indicated that Ce-PA possessed an average particle size of 185 nm, demonstrating good monodispersity and thermal stability. Furthermore, Ce-PA exhibited excellent dispersibility within the epoxy matrix and endowed the coatings with favorable mechanical properties. The Ce-PA leachate effectively protected aluminum alloy from corrosive media, achieving a protection efficiency of 98.7%. Specifically, the coating formulation incorporating 4% Ce-PA preserved a coating resistance of 1.0×10^8 Ω·cm² following 50 days of immersion in 3.5 wt% NaCl solution. Even for coatings with artificial defects, the resistance remained at 7.5×10^6 Ω·cm² after 14 days of exposure. In aqueous environments, Ce-PA released Ce^{4+} and PA^{n-} ions, which collectively formed a composite protective layer comprising a phytic acid conversion coating and $Ce(OH)_4$ deposits on the aluminum substrate, thereby markedly improving the corrosion resistance of the epoxy coating system.

Keywords: *aluminum alloy; cerium phytate; epoxy coatings; electrochemical impedance; corrosion resistance; functional materials*

Received on 15 Feb 2026, Accepted on 15 May 2026, Published on 22 July 2026

1 Introduction

Aluminum alloys possess excellent corrosion resistance and fatigue resistance, and have been widely applied in aerospace, shipbuilding, and other fields [1-6]. A compact passive oxide layer develops spontaneously on aluminum surfaces upon atmospheric exposure, providing substrate protection against corrosive attack. Nevertheless, this passive film is susceptible to rupture under humid or aggressively corrosive conditions, compromising its protective functionality. Alternative corrosion mitigation strategies for aluminum alloys predominantly encompass chemical conversion treatments [7], sol-gel deposition [8], anodization [9], and organic coating systems [10]. Epoxy coatings offer high mechanical strength, excellent adhesion to metal substrates, and good chemical corrosion resistance, making them prevalent in metal anti-corrosion applications. Nevertheless, unmodified epoxy coatings are incapable of delivering sustained metallic substrate protection, thereby necessitating the incorporation of active corrosion-inhibiting pigments to enhance long-term durability.

Phytic acid (PA) is an organic polyacid extracted from plants. Its multiple phosphate groups exhibit strong chelating ability, forming water-insoluble chelates with metal ions to protect metals from corrosive media [11]. Liu et al. [12] investigated the impact of chemical conversion treatments conducted in diverse phytic acid solutions on the corrosion behavior of Al-Cu-Mg alloy. Their observations revealed that films generated in phytic acid/zinc ion and phytic acid/manganese ion media exhibited superior compactness and structural integrity compared with those formed in pure phytic acid, consequently yielding substantially elevated corrosion potentials and diminished corrosion current densities. Shi et al. [13] assessed the protective effectiveness of phytic acid conversion coatings on 2024-T3 aluminum alloy. Their findings indicated that coatings fabricated within the pH range of 3.0–5.5 delivered satisfactory corrosion protection, whereas excessively acidic conditions

promoted hydrogen evolution, thereby hindering the formation of stable and dense protective films. Yang et al. [14] developed a dual pretreatment strategy to enhance the corrosion resistance of carbon steel in simulated concrete pore solutions. Through combined protection via phytic acid conversion films and molybdate inhibitors, electrochemical characterization confirmed that the dual-pretreated carbon steel exhibited corrosion resistance improvements of 99.0% and 102.3% relative to single phytic acid and single molybdate pretreatments, respectively. Morphological and compositional analyses revealed that phytic acid anchored to the iron substrate through chelation, while molybdate species permeated through microdefects in the phytic acid film to react with the substrate, forming $Fe_2(MoO_4)_3$/$FeMoO_4$ phases—demonstrating a pronounced synergistic protective effect. Additionally, phytic acid can generate dense conversion films on aluminum and magnesium alloys, providing effective protection. Cerium ions can form cerium salt conversion films on aluminum surfaces, effectively inhibiting corrosion [15-16]. Zhang et al. [17] formed conversion films on Al-Zn-Mg-Cu alloy via cerium salt surface treatment and examined its corrosion resistance in chloride-containing environments. Potentiodynamic polarization, free corrosion potential monitoring, and immersion tests indicated that cerium treatment significantly improved the alloy's resistance to pitting and uniform corrosion. The cerium salt conversion film delayed both anodic and cathodic reaction processes. SEM images revealed a bilayer structure formed by two different treatment steps, with a crack-like network on the surface. Bethencourt et al. [18] explored methods to protect AA2017 aluminum alloy from corrosion in NaCl aqueous solutions via thermal treatment and chemical activation in cerium-containing solutions. SEM/EDS characterization revealed the formation of a heterogeneous surface layer comprising an aluminum oxide/hydroxide film with cerium dispersed across cathodic metallic phases on the alloy substrate.

This study intends to combine phytic acid and cerium ions to prepare bio-based nano-cerium phytate (Ce-PA). Based on these findings, epoxy composite coatings were subsequently formulated. The corrosion inhibition mechanism of nano-Ce-PA dispersed within epoxy matrices was systematically investigated through electrochemical impedance spectroscopy, potentiodynamic polarization measurements, and salt spray exposure evaluations. It is envisaged that nano-Ce-PA will synergistically amalgamate the protective functionalities of phytic acid and cerium ions, conferring exceptional corrosion resistance upon epoxy coating systems.

2 Experimental Section

2.1 Materials, Reagents, and Instruments

AA2024 aluminum alloy was supplied by China Aluminum Corporation. Epoxy resin (901-75X, industrial grade) was purchased from Nan Ya Epoxy Resin Co., Ltd. Phytic acid (70 wt%) and cerium nitrate hexahydrate (analytical grade) were sourced from Shanghai Macklin Biochemical Technology Co., Ltd. Curing agent 8115 (industrial grade) was sourced from Shanghai Jiangqiao Chemical Co., Ltd.

A JSM-IT800 field emission scanning electron microscope was employed for microstructural characterization. Fourier transform infrared spectroscopic analysis was conducted on a NEXUS 470 spectrometer. Thermogravimetric characterization was performed using a STA 449C simultaneous thermal analyzer. All electrochemical measurements were executed on an Autolab 302N potentiostat.

2.2 Preparation of Ce-PA and Coatings

The preparation process of Ce-PA nanoparticles and the epoxy coating is illustrated schematically in Fig. 1.

At room temperature, 100 mL of cerium nitrate solution (0.15 mol/L) and 100 mL of phytic acid solution (0.1 mol/L) were prepared. A phytic acid solution was gradually introduced dropwise into a cerium nitrate solution maintained under vigorous agitation at a controlled rate of 1 drop per second via syringe delivery. The milky-white precipitate that formed was recovered by vacuum filtration, subjected to successive rinsing with deionized water until the effluent attained neutrality, and subsequently dehydrated under reduced pressure to afford a white powdered product designated as Ce-PA.

Aluminum alloy substrates were sequentially abraded with 400, 800, and 1200 grit sandpapers, followed by cleaning and desiccation for subsequent processing. Five grams of Ce-PA were dispersed in 20 mL xylene via

ultrasonication for 20 min. Upon achieving homogeneous suspension, the dispersion was incorporated into epoxy resin at mass fractions of 2%, 4%, 6%, 8%, and 10% relative to epoxy resin mass, yielding corresponding coating formulations. These paints were applied onto polished AA2024 substrates using a wire-wound drawdown bar. Following room-temperature curing for 24 h and subsequent thermal curing at 60 °C for 12 h, the as-prepared Ce-PA composite coatings displayed an average thickness of 65 μm. The corresponding formulations were denoted as EP-2, EP-4, EP-6, EP-8, and EP-10, respectively. A pristine epoxy coating devoid of Ce-PA was prepared as a reference control, designated EP.

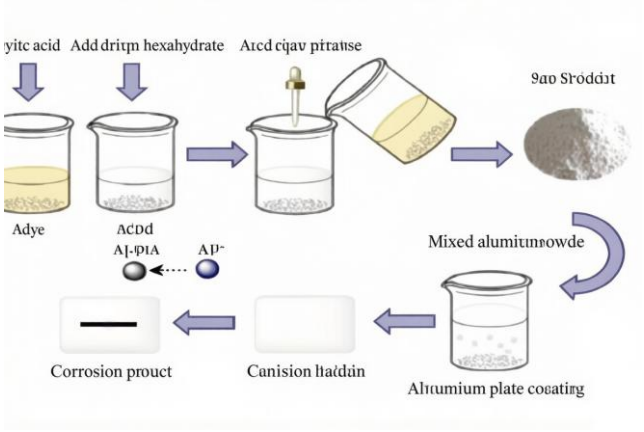

Figure 1 Schematic diagram of preparation process of Ce-PA nanoparticles and coating

2.3 Characterization and Performance Testing

SEM imaging was executed in secondary electron detection mode with a beam current of 20 μA and accelerating potential of 15.0 kV. FTIR measurements were performed over a wavenumber span of 4000 to 400 cm^{-1}, employing a spectral resolution of 4 cm^{-1} and signal averaging across 32 scans. For TGA, the samples were heated from ambient temperature (25 °C) up to 700 °C under a steady nitrogen flow of 15 mL/min, with the temperature ramp set at 10 °C per minute. The coated panels were further subjected to a series of mechanical performance tests: bending flexibility was assessed per GB/T 6742-2007, impact durability per GB/T 1732-2020, cross-hatch adhesion per GB/T 9286-2021, and surface hardness per GB/T 6739-2022.

Electrochemical characterization was performed in a three-electrode configuration, with the aluminum alloy substrate or coated specimen serving as the working electrode, a saturated calomel electrode as the reference, and a platinum sheet as the auxiliary electrode. Potentiodynamic polarization scans were executed from -0.2 V to +0.2 V relative to the open circuit potential at a sweep rate of 1 mV/s. Electrochemical impedance spectroscopy was acquired over the frequency range of 0.01 Hz to 1.0×10^5 Hz with a perturbation amplitude of 20 mV. The exposed test area was 19.6 cm^2. Both polarization and impedance measurements were conducted in 3.5 wt% sodium chloride solution. Impedance data were analyzed using Zsimpwin 3.1 software.

For the leaching inhibition assessment of Ce-PA, 50 mg of Ce-PA was dispersed in 100 mL of 3.5 wt% NaCl solution and agitated for 24 h to prepare the leaching solution. Subsequently, polished aluminum specimens were immersed in the obtained leachate for various time intervals. The metal protection efficiency (η) was calculated according to Equation (1):

η/%=icorr0icorr0−icorr×100(1)

Where ηis the protection efficiency (%); icorr0and icorrare the corrosion current densities of aluminum alloy immersed in 3.5 wt% NaCl solution and Ce-PA leachate, respectively [19] (μA/m^2).

To assess the protective performance of epoxy coatings under compromised conditions, an artificial scribe was intentionally introduced to expose the underlying bare substrate. These defective specimens were subsequently subjected to immersion testing in 3.5 wt% NaCl solution. The ability of Ce-PA to inhibit corrosion propagation at

the damaged sites was investigated through electrochemical impedance spectroscopy and open circuit potential monitoring over time.

Neutral salt spray tests were conducted according to ASTM B117-2019. The solution was 5 wt% NaCl at 35 °C. Prior to testing, a scratch exposing the substrate was made on the sample surface.

3 Results and Discussion

3.1 Characterization of Samples

3.1.1 FTIR Analysis

Fig. 2 shows the FTIR spectrum of Ce-PA.

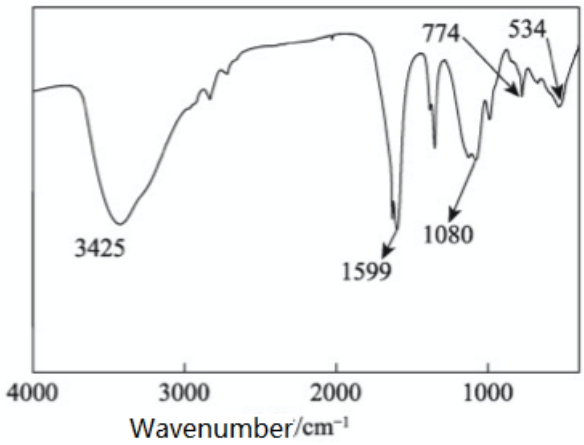

Figure 2 FTIR spectrum of Ce-PA

Absorption features at 3425, 1599, and 1080 cm^{-1} are assigned to hydroxyl stretching [20], phosphate P–O asymmetric stretching [21], and phosphoryl P=O stretching [22], respectively. Bands at 774 and 534 cm^{-1} correspond to cerium-oxygen bond stretching vibrations [23]. This spectroscopic evidence collectively confirms successful Ce-PA synthesis.

3.1.2 TGA Analysis

Fig. 3 displays the TGA and DTG curves of Ce-PA.

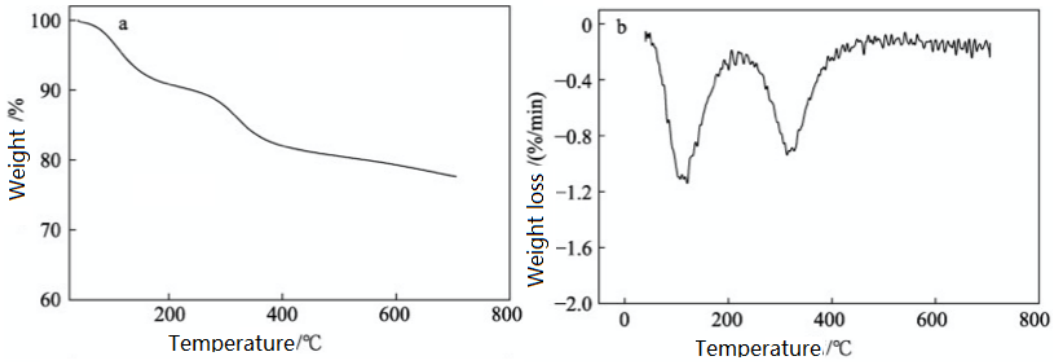

Figure 3 TGA (a) and DTG (b) curves of Ce-PA

The TGA curve for Ce-PA reveals two well-defined mass loss events. The initial decline from ambient temperature to approximately 200 °C is associated with the removal of adsorbed and coordinated water molecules from the

Ce-PA structure. A pronounced and steep mass reduction centered around 300 °C reflects the thermal degradation of the organic phosphate framework. Collectively, these observations indicate that Ce-PA possesses satisfactory thermal stability under the investigated conditions.

3.1.3 SEM Analysis

Fig. 4 presents the cross-sectional SEM images of Ce-PA and the epoxy coatings (EP-2 to EP-10).

As illustrated in Fig. 4a, Ce-PA demonstrates favorable dispersibility, with a mean particle diameter of 185 nm. The surface of the neat EP coating appears smooth (Fig. 4b). At lower Ce-PA loadings (2%–6%), the nanoparticles are uniformly dispersed within the epoxy matrix (Fig. 4c–e). However, as the loading increases to 8% and 10%, agglomeration of Ce-PA becomes evident (Fig. 4f, g). Agglomeration introduces defects into the coating, thereby compromising its corrosion resistance.

3.2 Inhibition Effect of Ce-PA Leachate on Aluminum

Fig. 5 presents the potentiodynamic polarization profiles and electrochemical impedance spectra of aluminum alloy specimens immersed in Ce-PA leachate and 3.5 wt% NaCl solution. The polarization curve fitting parameters are compiled in Table 1. EIS data were analyzed using the equivalent circuit depicted in Fig. 5d, with fitting results summarized in Table 2.

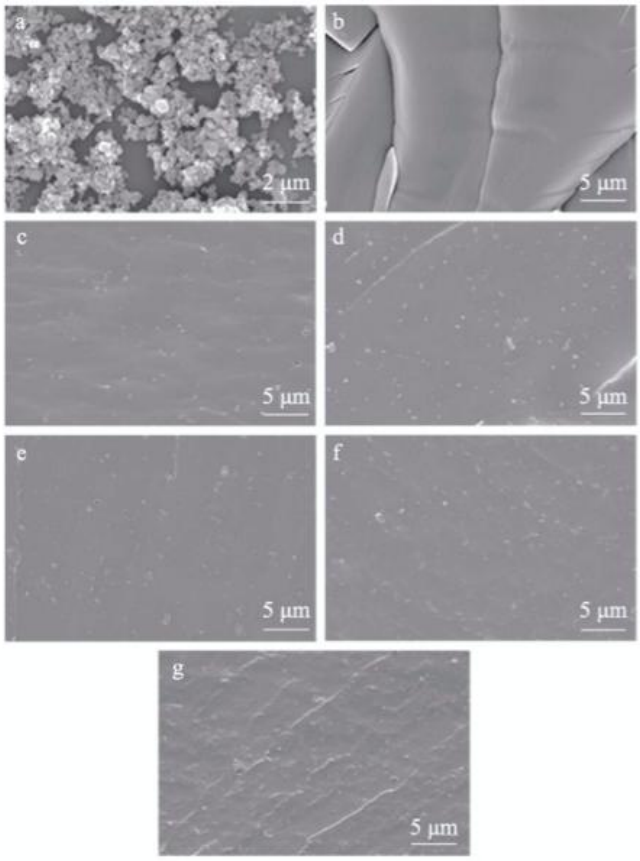

Figure 4 Cross-section SEM images of Ce-PA (a), EP coating (b), EP-2 (c), EP-4 (d), EP-6 (e), EP-8 (f), EP-10 (g)

The results compiled in Table 1 reveal a pronounced decrease in corrosion current density accompanied by a distinct positive displacement of the corrosion potential for the aluminum alloy sample after treatment with the Ce-PA leaching solution. Following 8 h of immersion, the inhibition efficiency attained 97.4%. Prolonging the immersion duration to 24 h elevated the efficiency further to 98.7%, demonstrating that the nano-Ce-PA leachate exerts effective corrosion suppression on aluminum alloy in 3.5 wt% NaCl solution.

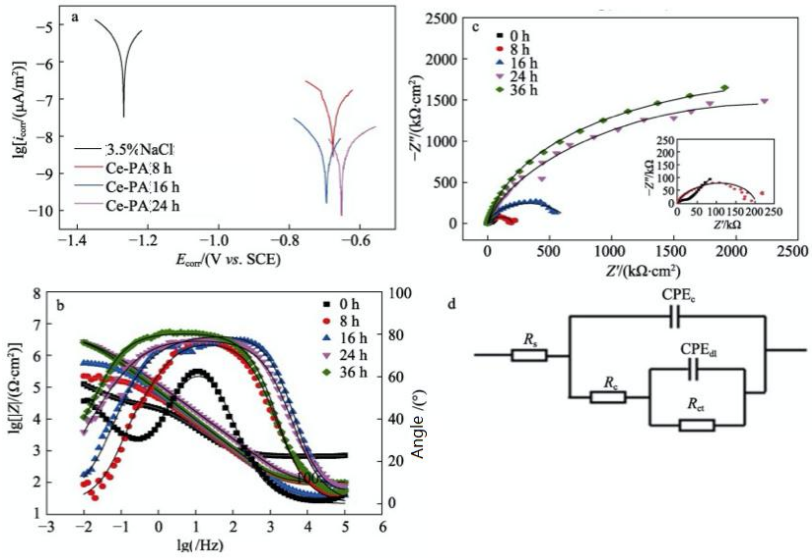

Figure 5 Polarization curves (a), Bode plots (b), and Nyquist plots (c) of aluminum alloy immersed in the extract of Ce-PA and mass fraction of 3.5% NaCl solution; Equivalent electrical circuit used to fit the EIS curves (d)

Table 1 Fitted polarization parameters and inhibition efficiency of AA2024 aluminum alloy immersed in Ce-PA leaching solution

Immersion solution	Ecorr/ (V vs. SCE)	icorr/ (μA/m²)	−bc/ (mV/dec)	ba/ (mV/dec)	η/ %
3.5 wt% NaCl solution 0 h	-1.268	2.3×10^{-8}	55	36	—
Ce-PA leachate 8 h	-1.077	1.9×10^{-9}	36	35	97.4
Ce-PA leachate 16 h	-0.695	8.3×10^{-9}	229	19	98.6
Ce-PA leachate 24 h	-0.653	9.7×10^{-9}	29	27	98.7

Note: "—" indicates no data available; bcand baare Tafel slopes exported from fitting software.

In Table 2, Rc and Rct represent the coating resistance and charge transfer resistance, respectively; CPEc and CPEdl correspond to the coating capacitance and double-layer capacitance, respectively; $|Z|_{0.01}$Hz denotes the impedance modulus at the low-frequency limit; and nc and ndl are the dispersion exponents associated with the coating and double-layer capacitance, respectively. As the immersion period extends, Rc shows a progressive increase. After 24 h of immersion, Rc rises by approximately two orders of magnitude relative to the initial value, which is indicative of excellent corrosion inhibition performance.

Table 2 Fitted results of impedance parameters of AA2024 aluminum alloy immersed in Ce-PA leaching solution

Immersion solution	Yc/ (F·S^{n-1}/cm²)	nc	Rc/ (Ω·cm²)	Ydl/ (F·S^{n-1}/cm²)	ndl	Rct/ (Ω·cm²)	$
3.5 wt% NaCl solution	5.9×10^{-6}	0.84	3.0×10^{4}	5.1×10^{-5}	0.84	3.0×10^{4}	1.2×10^{5}
Ce-PA leachate 8 h	3.9×10^{-6}	0.86	1.5×10^{5}	1.1×10^{-5}	1.00	5.7×10^{4}	2.2×10^{5}

Ce-PA leachate 16 h	1.2×10^{-6}	0.64	6.7×10^{5}	2.6×10^{-6}	0.91	3.0×10^{5}	5.6×10^{5}
Ce-PA leachate 24 h	1.7×10^{-6}	0.86	1.7×10^{6}	1.6×10^{-6}	0.62	2.8×10^{6}	2.7×10^{6}

Note: Ycand Ydlare constants of the constant phase element (CPE).

Fig. 6 shows SEM images of the aluminum alloy surface after immersion in 3.5 wt% NaCl solution and Ce-PA leachate for different durations.

As illustrated in Fig. 6, the aluminum surface developed numerous corrosion pits following merely 2 h of exposure to 3.5 wt% NaCl solution. Conversely, specimens immersed in Ce-PA leachate exhibited complete absence of pitting attack. With progressive NaCl immersion duration, pitting corrosion intensified markedly, culminating in extensive pit formation. Conversely, when immersed in Ce-PA leachate, not only are no pits observed, but a dense protective film forms on the surface over time, effectively shielding the aluminum from corrosion. This finding aligns well with the results obtained from polarization curve and EIS measurements.

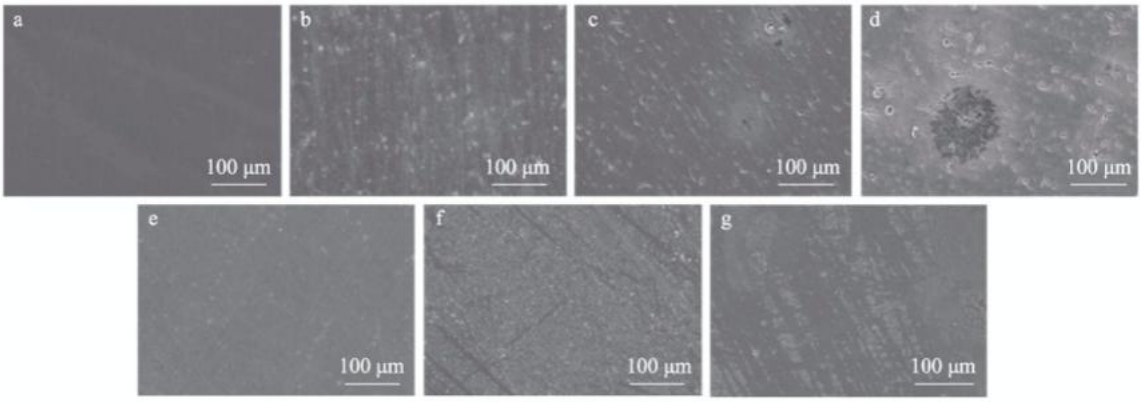

Figure 6 SEM images of AA2024 aluminum alloy immersed in mass fraction 3.5% NaCl solution for 0 h (a), 2 h (b), 16 h (c), 24 h (d), as well as immersed in Ce-PA leaching solution for 2 h (e), 16 h (f), 24 h (g)

Table 3 presents the EDX data of AA2024 aluminum alloy after 24 h of immersion in Ce-PA leachate.

Table 3 EDX data of AA2024 aluminum alloy immersed in Ce-PA leaching solution for 24 h

Element	Atomic number	Mass fraction / %	Atomic percentage / %
Al	13	94.33	92.04
O	8	4.24	6.98
P	15	1.08	0.92
Ce	58	0.34	0.06

The sample contains P and Ce elements, indicating that Ce-PA hydrolyzes in water, releasing phytate anions and cerium ions, which eventually form a composite protective film on the aluminum surface, effectively inhibiting corrosion.

3.3 Mechanical Properties of Coatings

Table 4 lists the mechanical properties of different coatings.

Table 4 Mechanical properties of different coatings

Coating	Pencil hardness / H	Flexibility / mm	Impact strength / (kg·cm)	Adhesion / Grade
EP	2	1	50	0
EP-2	2	1	50	0
EP-4	2	1	50	0
EP-6	2	1	50	0
EP-8	2	1	50	0
EP-10	2	1	50	0

As shown in Table 4, the addition of nano-Ce-PA to the epoxy coating does not significantly alter the pencil hardness, flexibility, impact resistance, or adhesion of EP-2 to EP-10. This is primarily attributed to the small particle size of nano-Ce-PA, which allows for uniform dispersion within the epoxy matrix. Even at a high loading of 10%, the mechanical properties of the epoxy coating are not compromised.

3.4 Corrosion Resistance Analysis of Intact Coatings

Open circuit potential is commonly utilized as an initial criterion for evaluating the corrosion protective capability of coatings [24–25]. Fig. 7 depicts the time-dependent variation of open circuit potential for diverse epoxy coating systems throughout 50 days of immersion in 3.5 wt% NaCl solution.

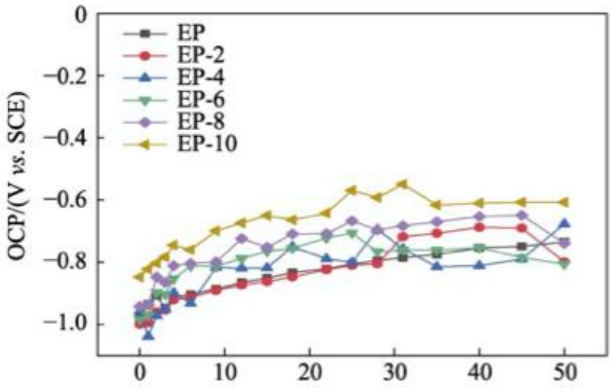

Figure 7 OCP of different coatings immersed in mass fraction 3.5% NaCl solution for different time

The OCP values of the epoxy coatings exhibit a gradual upward trend with increasing Ce-PA content. The EP-10 formulation (10% Ce-PA) demonstrates the highest OCP, implying that elevated Ce-PA loading is conducive to improving the OCP of the coating system.

Bode and Nyquist diagrams for the various coating systems following immersion in 3.5 wt% NaCl solution for 0, 7, 15, 30, and 50 days are illustrated in Fig. 8 and Fig. 9, respectively. The equivalent circuit models employed for fitting the acquired EIS data are depicted in Fig. 10, with the corresponding fitted parameters compiled in Table 5, where Rs denotes the electrolyte resistance.

The low-frequency impedance modulus $|Z|_{0.01Hz}$ serves as a standard metric for assessing overall coating protective performance, with elevated values signifying superior corrosion resistance [26-27]. The data

presented in Table 5 reveal that the low-frequency impedance modulus ($|Z|_{0.01Hz}$) of the pristine EP coating declined from an initial value of 1.6×10^8 Ω·cm² to 7.1×10^7 Ω·cm² following 7 days of immersion. Upon prolonged exposure for 50 days, this parameter further diminished to 6.9×10^6 Ω·cm², signifying a substantial deterioration in barrier protection. By comparison, the nano-Ce-PA-modified coatings consistently exhibited markedly elevated $|Z|_{0.01Hz}$ values relative to the neat EP counterpart. As a representative example, the EP-4 formulation displayed an initial rise in $|Z|_{0.01Hz}$ during the early immersion phase and subsequently maintained a stable value on the order of 1.0×10^8 Ω·cm² throughout the entire 50-day testing period, thereby confirming its outstanding long-term corrosion resistance. However, the anti-corrosion performance decreases as the Ce-PA loading increases further, such as in EP-6 and EP-8. This is due to the agglomeration of Ce-PA at higher loadings, which introduces defects and weakens the coating's barrier properties. Interestingly, when the Ce-PA content rises to 10%, the coating regains good corrosion resistance, with 丨Z丨0.01Hzstabilizing at 3.0×108Ω·cm2after 50 days of immersion.

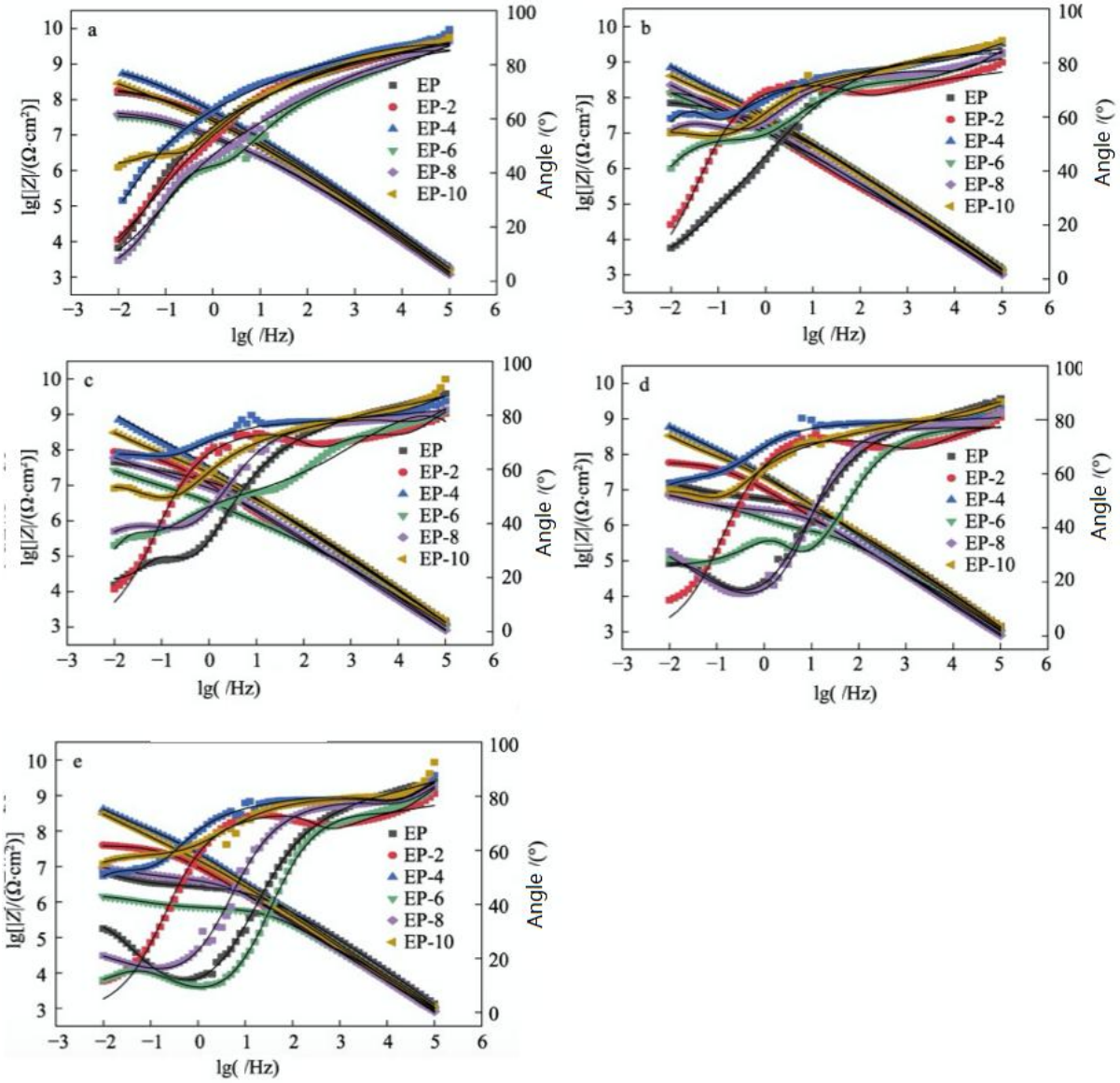

Figure 8 Bode plots of different coatings immersed in mass concentration 3.5% NaCl solution for different time

CPEc is often used to characterize the anti-permeability of a coating [28], and it typically increases with continuous water penetration. From Table 5, the CPEcof the EP coating rises to 6.9×10−8F·Sn−1/cm2after 50 days of immersion. In contrast, the CPEcof coatings with nano-Ce-PA shows a relatively lower increasing rate.

The CPEcof EP-4 remains at 7.3×10−9F·Sn−1/cm2after 50 days, the lowest among all coatings, indicating excellent impermeability.

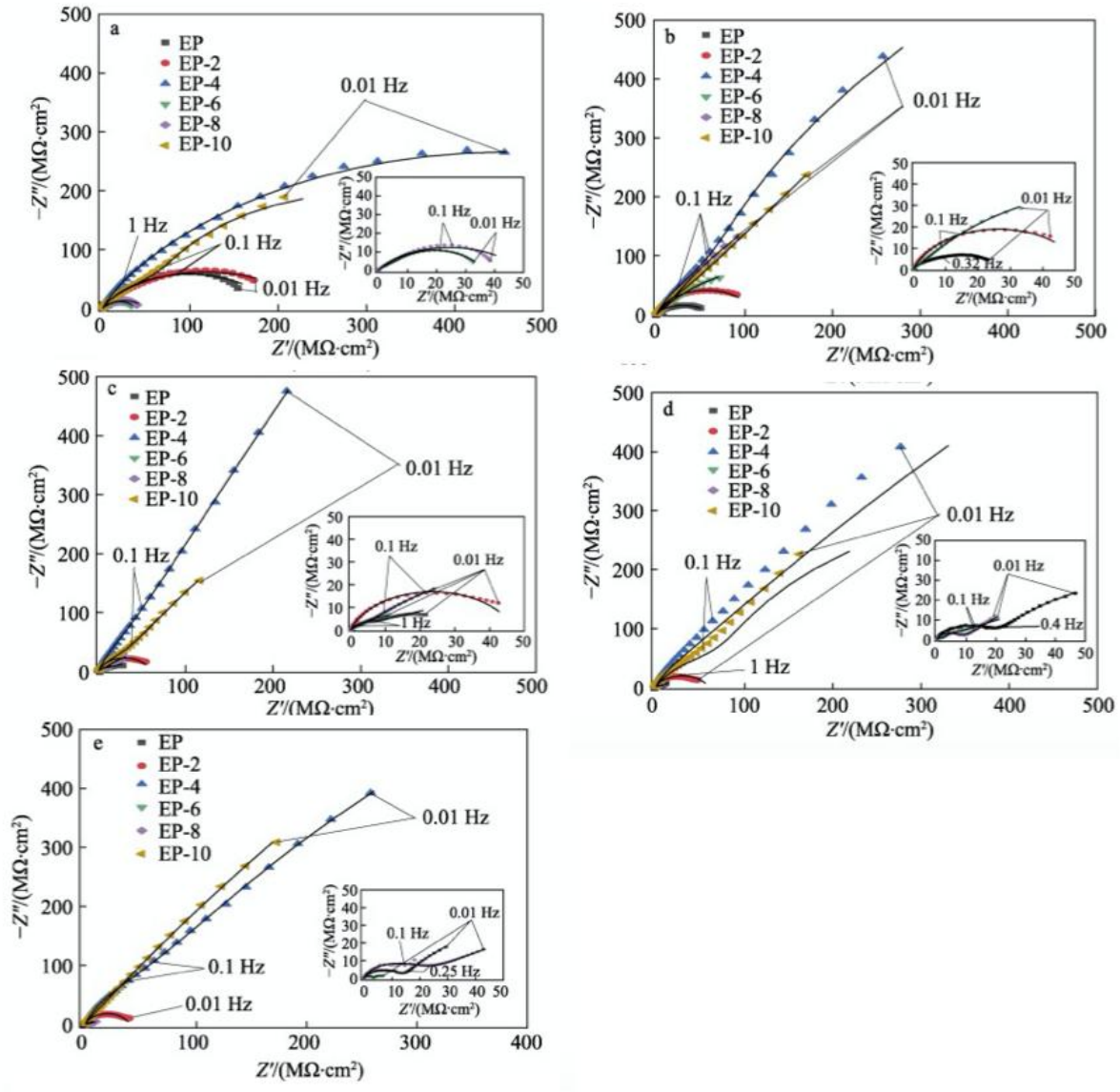

Figure 9 Nyquist plots of different coatings immersed in mass fraction 3.5% NaCl solution at different immersion time

Rc serves as a standard metric for characterizing the corrosion resistance of coatings, wherein elevated values correspond to enhanced protective performance [29]. The data in Table 5 indicate that the Rc of the unmodified EP coating dropped precipitously from an initial 2.0×10^{8} Ω·cm² to 9.1×10^{7} Ω·cm² within merely 7 days, signifying a marked decline in barrier protection. Conversely, all Ce-PA-incorporated formulations demonstrated Rc values surpassing that of the pristine EP coating. Furthermore, as the immersion period extended, the Rc of Ce-PA-modified systems generally displayed an initial decrease followed by a recovery, suggesting that Ce-PA possesses the capacity to autonomously repair micro-defects in the coating matrix and consequently bolster corrosion resistance. Particularly noteworthy is that the Rc of EP-4 remained at 5.9×10^{8} Ω·cm² after 50 days of exposure, representing an improvement of two orders of magnitude over EP and substantially exceeding all other compositions, thereby corroborating its outstanding corrosion protective efficacy. Additionally, the Rctof the EP coating shows minimal increase during the immersion period, indicating that the generated aluminum corrosion products fail to provide effective protection. In contrast, the Rctof Ce-PA-added coatings increases substantially,

indicating that Ce-PA effectively inhibits the penetration of corrosive media. The Rctof EP-4 fluctuates minimally and remains the highest throughout the immersion period, outperforming other coatings. The double-layer capacitance CPEdlreflects the anti-delamination performance of the coating [30]. After adding nano-Ce-PA, the CPEdlof epoxy coatings shows a gradual decreasing trend during immersion. Particularly, the CPEdlof EP-4 remains at a low value of 1.9×10−9F · Sn−1/cm2after 50 days, indicating good anti-delamination performance.

Table 5 Fitted parameters of EIS curves for complete coatings

Immersion time / d	Coating	Yc/ ($F \cdot S^{n-1}/cm^2$)	nc	Rc/ ($\Omega \cdot cm^2$)	Ydl/ ($F \cdot S^{n-1}/cm^2$)	ndl	Rct/ ($\Omega \cdot cm^2$)	$
0	EP	1.4×10^{-9}	0.98	2.0×10^{8}	9.7×10^{-9}	0.63	6.5×10^{4}	1.6×10^{8}
	EP-2	1.7×10^{-9}	0.95	2.5×10^{8}	8.5×10^{-9}	0.55	2.7×10^{5}	1.8×10^{8}
	EP-4	1.2×10^{-9}	0.97	9.6×10^{8}	4.8×10^{-9}	0.61	3.9×10^{5}	5.6×10^{8}
	EP-6	2.1×10^{-9}	0.96	1.4×10^{7}	3.5×10^{-8}	0.53	2.5×10^{4}	3.3×10^{7}
	EP-8	2.3×10^{-9}	0.96	9.3×10^{7}	2.9×10^{-8}	0.56	2.4×10^{4}	3.9×10^{7}
	EP-10	2.3×10^{-9}	0.94	3.9×10^{9}	1.3×10^{-8}	0.49	2.8×10^{5}	2.8×10^{8}
7	EP	2.8×10^{-8}	0.93	9.1×10^{7}	1.5×10^{-8}	0.45	2.1×10^{5}	7.1×10^{7}
	EP-2	1.1×10^{-8}	0.85	1.6×10^{8}	9.1×10^{-8}	0.75	2.9×10^{5}	1.4×10^{8}
	EP-4	2.6×10^{-9}	0.93	3.6×10^{8}	6.6×10^{-9}	0.60	2.2×10^{5}	7.1×10^{8}
	EP-6	6.9×10^{-9}	0.88	4.1×10^{7}	2.8×10^{-8}	0.50	7.1×10^{5}	1.3×10^{8}
	EP-8	1.1×10^{-8}	0.85	2.3×10^{9}	1.9×10^{-8}	0.61	1.6×10^{7}	2.3×10^{8}
	EP-10	3.2×10^{-9}	0.92	1.1×10^{9}	9.6×10^{-9}	0.52	3.5×10^{5}	4.1×10^{8}
15	EP	3.5×10^{-8}	0.91	1.5×10^{8}	3.7×10^{-8}	0.30	2.7×10^{5}	4.5×10^{7}
	EP-2	1.9×10^{-8}	0.80	3.0×10^{7}	1.3×10^{-7}	0.99	9.2×10^{5}	8.8×10^{7}
	EP-4	4.1×10^{-9}	0.91	9.9×10^{8}	4.9×10^{-9}	0.61	2.1×10^{6}	8.4×10^{8}
	EP-6	1.1×10^{-8}	0.86	7.3×10^{7}	1.1×10^{-7}	0.48	1.8×10^{5}	2.6×10^{7}
	EP-8	1.2×10^{-8}	0.86	4.3×10^{8}	6.4×10^{-8}	0.50	8.6×10^{6}	6.0×10^{7}
	EP-10	3.3×10^{-9}	0.92	1.5×10^{8}	1.1×10^{-8}	0.49	1.5×10^{6}	3.1×10^{8}
30	EP	6.1×10^{-8}	0.87	4.9×10^{6}	—	—	—	1.6×10^{7}
	EP-2	2.0×10^{-8}	0.80	1.4×10^{7}	1.3×10^{-7}	1.00	5.6×10^{7}	5.8×10^{7}
	EP-4	6.7×10^{-9}	0.83	3.5×10^{8}	5.7×10^{-9}	0.55	7.8×10^{7}	5.9×10^{8}

	EP-6	1.3×10^{-8}	0.85	1.5×10^{7}	3.2×10^{-7}	0.45	4.6×10^{5}	7.0×10^{6}
	EP-8	1.4×10^{-8}	0.86	2.4×10^{6}	—	—	—	6.9×10^{7}
	EP-10	4.3×10^{-9}	0.90	1.1×10^{8}	1.1×10^{-8}	0.49	2.6×10^{5}	3.3×10^{8}
50	EP	6.9×10^{-8}	0.86	2.3×10^{6}	—	—	—	6.9×10^{6}
	EP-2	8.3×10^{-8}	0.87	3.9×10^{7}	1.4×10^{-8}	0.75	4.9×10^{4}	4.0×10^{7}
	EP-4	7.3×10^{-9}	0.88	5.9×10^{8}	1.9×10^{-9}	0.54	5.0×10^{7}	4.1×10^{8}
	EP-6	1.4×10^{-8}	0.85	8.9×10^{6}	3.1×10^{-7}	0.43	4.1×10^{5}	5.4×10^{6}
	EP-8	1.4×10^{-8}	0.85	4.2×10^{6}	—	—	—	9.2×10^{6}
	EP-10	8.8×10^{-9}	0.87	1.1×10^{8}	1.3×10^{-8}	0.57	1.2×10^{7}	3.0×10^{8}

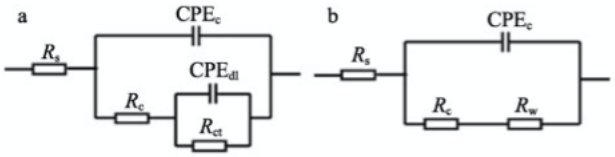

Figure 10 Equivalent electrical circuits

From Fig. 11, the OCP trend of defective coatings is opposite to that of intact coatings. EP-4 exhibits a relatively high OCP, while coatings with excessively high Ce-PA content (EP-8, EP-10) show lower OCP. This is likely because excessive Ce-PA increases coating defects; once damaged, corrosive media can easily penetrate through these defects, reducing protection. Conversely, insufficient Ce-PA cannot provide effective protection. The OCP of the EP coating is relatively high, possibly because aluminum corrosion products block the diffusion channels of corrosive media to some extent. Thus, OCP alone cannot determine the superiority of corrosion resistance; it must be combined with EIS. Throughout the immersion period, EP-4 consistently maintains the highest coating resistance (Rc=3.5×108to 9.9×108Ω·cm2) and the lowest coating capacitance (CPEc=1.2×10−9to 7.3×10−9F·Sn−1/cm2), demonstrating superior corrosion resistance and providing long-term protection for aluminum alloy.

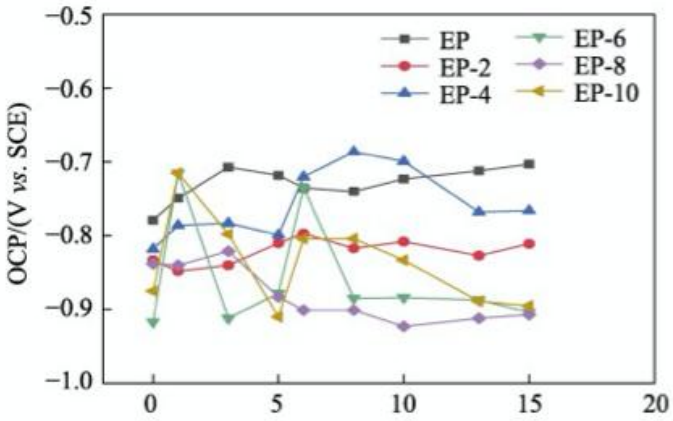

Figure 11OCP of coatings with artificial defects immersed in mass fraction 3.5% NaCl solution

3.5 Corrosion Resistance Analysis of Defective Coatings

Coatings often suffer mechanical damage during service. If the coating is damaged, the active pigments added must provide protection. Fig. 12 and Fig. 13 display the Bode and Nyquist plots for defective coatings after 14 days of immersion in 3.5 wt% NaCl solution. The electrochemical impedance data were fitted using the equivalent circuit shown in Fig. 10a, with the corresponding parameters summarized in Table 6.

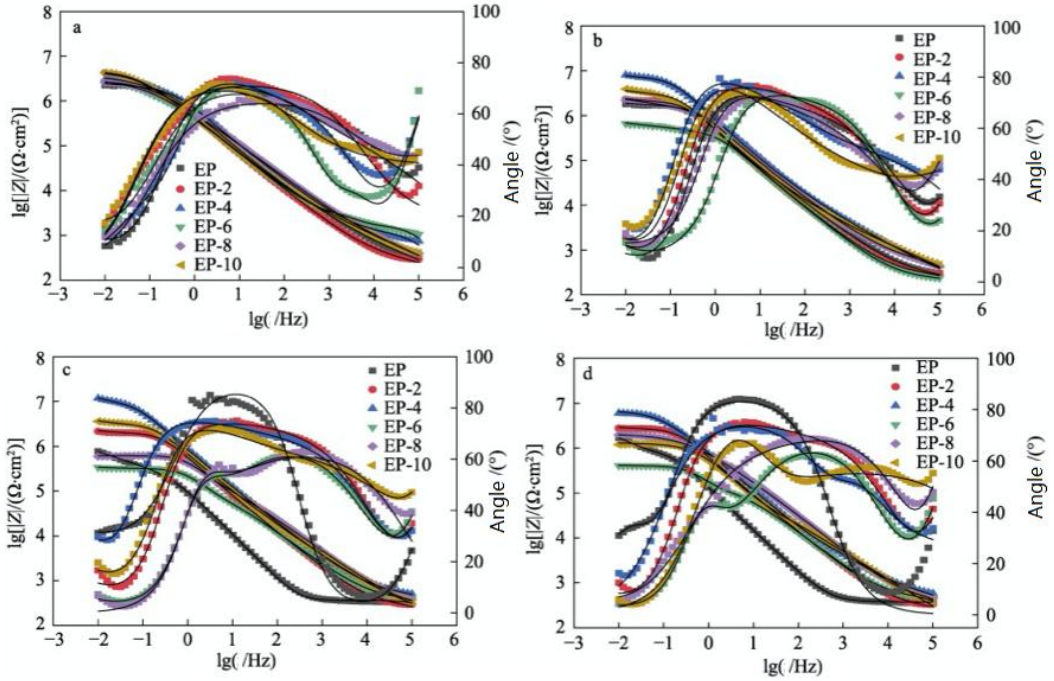

Figure 12Bode plots of coatings with artificial defects immersed in mass fraction 3.5% NaCl solution

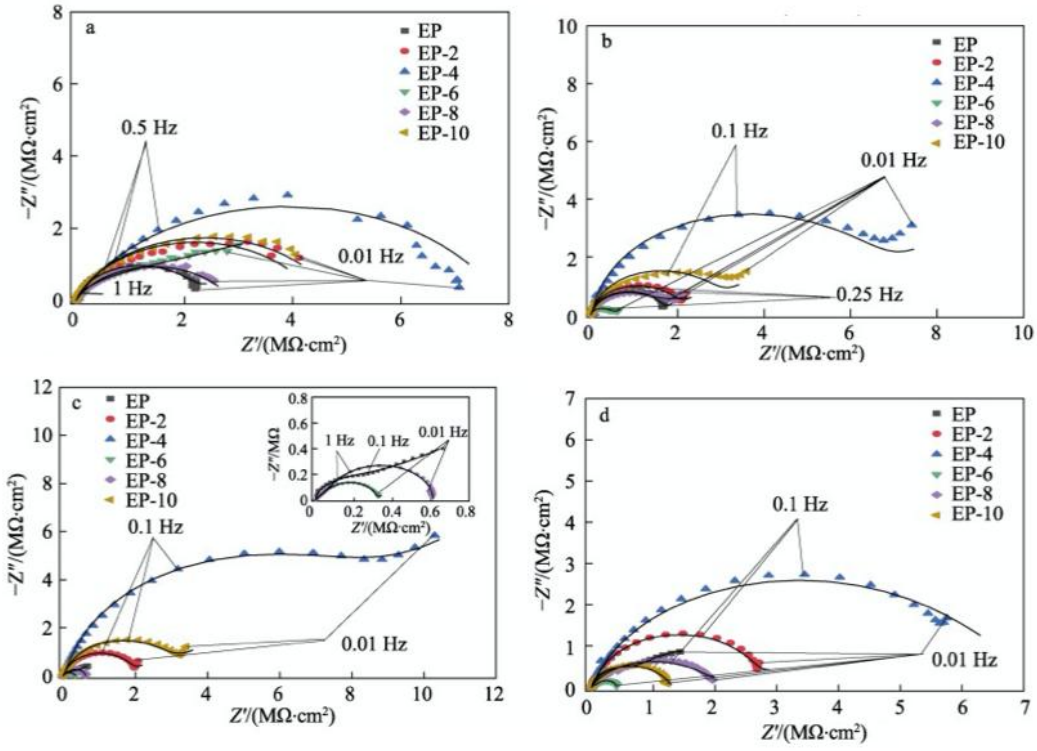

Figure 13 Nyquist plots of coatings with artificial defects immersed in mass fraction 3.5% NaCl solution

According to Table 6, the $|Z|_{0.01}$Hz values of all coatings undergo a sharp initial decline, attributable to the progressive penetration of NaCl solution through the artificial defect toward the coating–substrate interface. With extended immersion, the $|Z|_{0.01}$Hz of Ce-PA-containing coatings recovers to varying extents, signifying pronounced corrosion suppression at the damaged region. This phenomenon is ascribed to the formation of a protective film on the defect surface, which effectively shields the underlying substrate from corrosion attack—a morphological change also corroborated by the SEM micrographs of aluminum specimens exposed to the Ce-PA leaching solution. Particularly, the ｜Z｜0.01Hzof EP-4 remains at 6.0×106Ω·cm2after 14 days, significantly higher than other coatings, showing excellent corrosion resistance. Table 6 also shows that the Rcof the EP coating first increases and then decreases with immersion time, dropping to 1.7×106Ω·cm2after 14 days. Although corrosion products deposited at the defect can block NaCl diffusion to some extent, they are loose and cannot provide long-term protection. The Ce-PA content significantly impacts performance; both excessively high and low contents are detrimental. Overall, EP-4 exhibits the highest Rcvalue (7.5×106Ω·cm2) after 14 days, consistent with the results in Table 5.

Fig. 14 shows SEM images of defective coatings after 14 days of immersion in 3.5 wt% NaCl solution. Table 7 presents the corresponding EDX data.

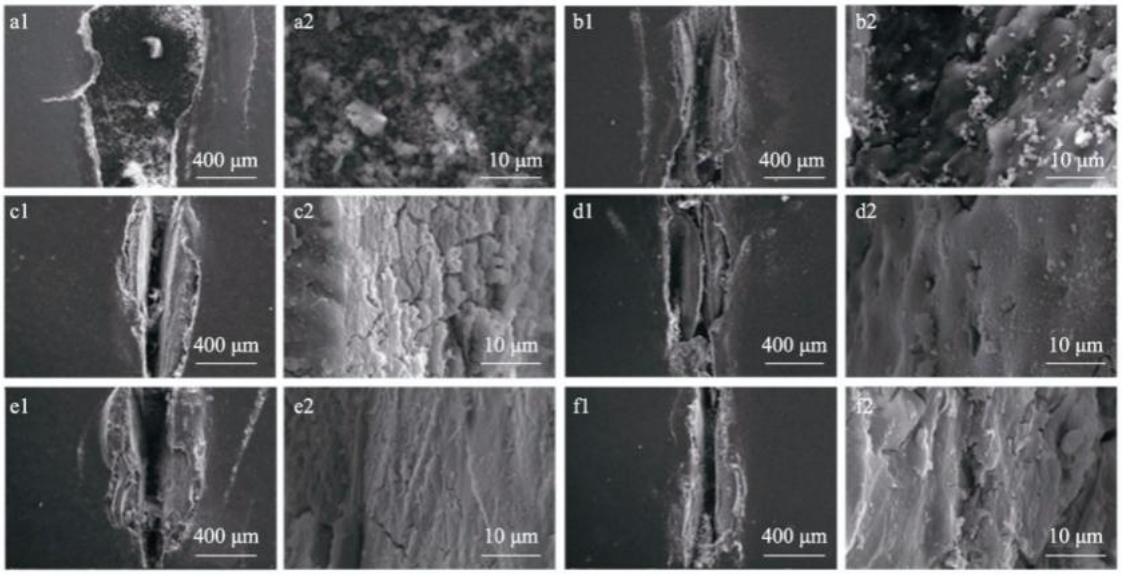

Figure 14 Surface (a1~f1) and inside (a2~f2) SEM images of coatings with artificial defects

Table 7 EDX data at the defect of coatings after 14 d immersion

Coating	Element	Atomic number	Mass fraction / %	Atomic percentage / %
EP	O	8	54.85	64.46
	Al	13	39.47	27.51
	C	6	4.84	7.58
	Cl	17	0.84	0.45
EP-2	O	8	49.33	62.50

	Al	13	44.76	33.63
	P	15	5.91	3.87
EP-4	Al	13	46.20	37.61
	O	8	38.78	53.24
	P	15	12.30	8.72
	Ce	58	2.72	0.43
EP-6	Al	13	65.17	55.01
	O	8	28.23	40.19
	P	15	6.50	4.78
	Ce	58	0.10	0.02
EP-8	Al	13	55.80	46.56
	O	8	33.50	47.14
	P	15	8.08	5.87
	Ce	58	2.63	0.42
EP-10	O	8	42.65	58.15
	Al	13	40.36	32.63
	P	15	11.98	8.44
	Ce	58	5.01	0.78

From Fig. 14, the defect surface of the EP coating is covered by loose aluminum corrosion products (Fig. 14a1). In contrast, the defect surfaces of Ce-PA-containing coatings are gradually covered by dense protective layers (Fig. 14b1~f1). According to Table 7, P element appears at the scratch of EP-2. As Ce-PA content increases, Ce element appears alongside P element at the scratches of EP-4, EP-6, EP-8, and EP-10. The contents of P and Ce first increase, then decrease, and then increase again with increasing Ce-PA content, consistent with the EIS trend. This is because the main corrosion process of aluminum in NaCl solution involves anodic dissolution, as shown in Eqs. (2)–(4). Additionally, nano-Ce-PA added to the coating hydrolyzes in water, releasing Ce^{4+} and phytate anions (PA^{n-}), as shown in Eq. (5). The released Ce^{4+} reacts with OH^- to form $Ce(OH)_4$ precipitate (Eq. 6), while PA^{n-} chelates with Al^{3+} to form $Al_n(PA)_3$ (Eq. 7). The generated $Al_n(PA)_3$ is dense and protects aluminum from corrosion, which is the main mechanism of phytic acid conversion films. $Ce(OH)_4$ further enhances the density of $Al_n(PA)_3$. However, excessive Ce-PA increases coating defects, making it difficult to achieve the desired effect. Combining electrochemical results with SEM/EDX data, EP-4 exhibits the best corrosion resistance, indicating that adding only 4% nano-Ce-PA to the epoxy coating achieves excellent performance. Compared with other anti-rust pigments, such as zinc phosphate (30%) [31] and ferrite (10%) [32], nano-Ce-PA offers the advantages of low loading (4%) and high efficiency.

Al→Al3++3e−(2)

2H2O+2e−→H2+2OH−(3)

Al3++3OH−→Al(OH)3↓(4)

Ce−PA→Ce4++PAn−(5)

Ce4++4OH−→Ce(OH)4↓(6)

PAn−+Al3+→Aln(PA)3↓(7)

3.6 Salt Spray Test Analysis

Fig. 15 shows the results of the salt spray test for different coatings.

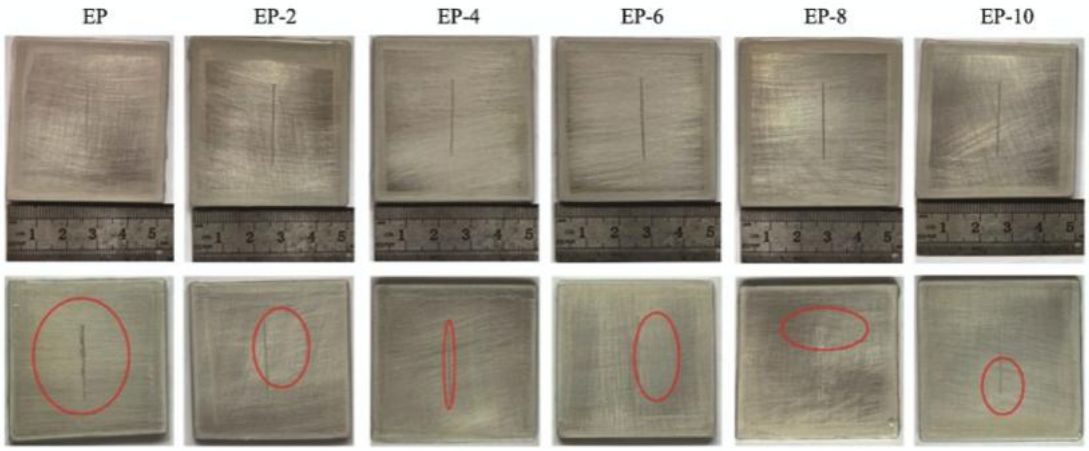

Figure 15 Optical photos of different coatings before and after 50 d salt spray test

Following 45 days of salt spray exposure, pronounced rust propagation was evident along both margins of the scribe defect on the EP coating, with the exposed substrate exhibiting complete loss of metallic luster. Noticeable water diffusion occurs in the marked red area. Since the coating is transparent, water diffusion is difficult to observe in the photos. In contrast, the corrosion expansion at the scratches of Ce-PA-containing coatings is significantly less severe than that of EP, retaining metallic luster. Particularly, EP-4 shows the smallest water diffusion area around the scratch, demonstrating excellent corrosion resistance.

4 Discussion

4.1 Molecular-Level Passivation Mechanisms, Chelation Chemistry, and the Thermodynamic Origin of Self-Healing Behavior

The exceptional corrosion inhibition performance reported for nano-cerium phytate (Ce-PA) cannot be adequately explained by conventional barrier theory alone; it emerges from a cascade of molecular-level interactions that collectively redefine the metal–electrolyte interface. At the heart of this mechanism lies the unique coordination chemistry of phytic acid (PA), a cyclohexane-based hexaphosphate with twelve dissociable protons and six phosphate groups arranged in a symmetrical array. This architecture grants PA an extraordinary chelation constant for trivalent and tetravalent metal ions, far exceeding that of conventional mono- or diphosphonate inhibitors. When Ce-PA nanoparticles encounter aqueous environments—either through direct leaching from the epoxy matrix or via capillary condensation at the coating–substrate interface—they undergo controlled hydrolysis, releasing Ce^{4+} cations and phytate anions (PA^{n-}). The thermodynamic driving force for this dissociation is modest, ensuring sustained release rather than burst depletion, a critical attribute for long-term protection. Once liberated, Ce^{4+} ions migrate toward cathodic sites on the aluminum alloy surface, where oxygen reduction generates localized alkaline conditions (pH > 8.5). Under these conditions, Ce^{4+} precipitates as $Ce(OH)_4$,

a highly insoluble cerium(IV) hydroxide that nucleates preferentially on intermetallic phases such as Al_2CuMg, effectively blocking cathodic reaction sites. Simultaneously, PA^{n-} anions diffuse toward anodic regions, where Al^{3+} ions are being ejected into solution. The phytate ligands coordinate with Al^{3+} through multidentate chelation, forming a cross-linked $Al_n(PA)_3$ network that is both mechanically robust and chemically inert. This dual-action passivation—cathodic blocking by $Ce(OH)_4$ and anodic chelation by $Al_n(PA)_3$—creates a composite conversion layer that is significantly more resilient than either component alone. Importantly, the formation of this layer is self-limiting: as coverage increases, the availability of reactive sites diminishes, slowing further deposition and preventing excessive buildup that could induce mechanical spalling. This intrinsic feedback loop explains the near-constant impedance modulus observed for EP-4 over 50 days of immersion and the absence of blistering or delamination in salt spray tests. The mechanism also accounts for the 98.7% inhibition efficiency recorded for aluminum coupons immersed in Ce-PA leachate, as the composite film not only physically isolates the substrate but also shifts the open-circuit potential anodically by more than 600 mV, placing the alloy firmly within the passive domain.

4.2 Dispersion Thermodynamics, Critical Pigment Volume Concentration, and the Non-Monotonic Performance Landscape

While the molecular inhibition mechanism is central to Ce-PA's efficacy, its macroscopic performance as an epoxy additive is governed by a delicate balance between dispersion quality, interfacial adhesion, and coating network integrity. The 185 nm average particle size of Ce-PA places it near the lower bound of the colloidal regime, where Brownian motion partially counteracts sedimentation but also increases the propensity for agglomeration via van der Waals forces. Successful incorporation therefore hinges on overcoming the interfacial energy mismatch between the hydrophilic, hydroxyl-rich Ce-PA surface and the hydrophobic epoxy matrix. Ultrasonic dispersion in xylene partially addresses this by disrupting pre-existing agglomerates, but long-term stability requires kinetic trapping of individual nanoparticles within the cross-linking epoxy network. At low loadings (2–4 wt%), Ce-PA particles are sufficiently separated to act as isolated nano-reservoirs, uniformly distributed and fully encapsulated by the polymer. This configuration maximizes the available surface area for controlled leaching while preserving the coating's barrier properties. However, as loading increases to 6–8 wt%, the interparticle distance shrinks below the critical pigment volume concentration (CPVC) threshold for this system. Particle–particle contacts proliferate, creating percolation pathways for water and chloride ions, and introducing micro-stress concentrators that weaken the epoxy network. The SEM micrographs of EP-8 and EP-10 vividly illustrate this transition: agglomerates appear as micron-scale nodules that disrupt the otherwise continuous polymer phase. Paradoxically, the EP-10 formulation recovers some corrosion resistance despite these defects, a phenomenon attributable to the sheer abundance of Ce-PA reservoirs. At 10 wt% loading, even if a fraction of particles are sequestered in agglomerates, the remaining dispersed fraction still releases sufficient inhibitor to sustain passivation. This explains the non-monotonic performance curve observed across the compositional series: corrosion resistance peaks at 4 wt%, declines at intermediate loadings due to agglomeration-induced defects, and partially rebounds at the highest loading due to excess inhibitor availability. Practically, this underscores that 4 wt% is the true optimum—delivering maximum protection with minimum additive burden, a crucial consideration for cost-sensitive industrial coatings.

4.3 Electrochemical Kinetics, Impedance Evolution, and the Role of Nano-Reservoirs in Defect Tolerance

The electrochemical impedance spectroscopy (EIS) data presented for both intact and artificially defective coatings provide profound insights into how Ce-PA transforms the dynamic response of the coating–metal system. For intact coatings, the low-frequency impedance modulus ($|Z|_{0.01}$ Hz) serves as a proxy for the overall resistance to ionic transport. In the pristine EP coating, $|Z|_{0.01}$ Hz decays exponentially over 50 days, reflecting progressive water uptake, plasticization, and ion ingress. In stark contrast, EP-4 exhibits an initial increase in $|Z|_{0.01}$ Hz during the first week, followed by stable maintenance near $10^8\ \Omega\cdot cm^2$. This counterintuitive initial rise is a hallmark of active inhibition: as trace amounts of Ce-PA leach into the coating–substrate interface, they initiate the formation of the $Al_n(PA)_3/Ce(OH)_4$ passivation layer, which adds an additional resistive barrier atop the aluminum surface. The constant phase element (CPE) parameters further corroborate this. The coating capacitance (CPEc) of EP-4 remains nearly an order of magnitude lower than that of EP throughout the test, indicating dramatically reduced water absorption. Meanwhile, the double-layer capacitance (CPEdl) stays suppressed, confirming that the passive layer remains thin and adherent rather than thickening into a porous, semi-conductive corrosion product

layer. For defective coatings, the role of Ce-PA shifts from prevention to containment. In the absence of inhibitor, corrosive species flood the scratch, triggering rapid pitting and undermining the surrounding coating. With Ce-PA present, the scratch itself becomes a delivery portal: electrolyte entering the defect dissolves nearby nanoparticles, generating a localized high concentration of inhibitor that precipitates directly within the damaged zone. The EIS data for EP-4 after 14 days of defect immersion reveal a coating resistance of 7.5×10^6 $\Omega \cdot cm^2$—orders of magnitude higher than the baseline—demonstrating that the nano-reservoirs actively "heal" the damaged area. This behavior aligns with the definition of a smart, self-healing coating, albeit one driven by passive leaching rather than encapsulated microcapsules. The EDX mapping of the scratch interior, showing enrichment of phosphorus and cerium, provides definitive proof of this in-situ repair mechanism.

4.4 Sustainability, Life-Cycle Positioning, and the Strategic Outlook for Bio-Based Anti-Corrosion Pigments

Beyond its technical performance, Ce-PA represents a significant advancement in the pursuit of sustainable corrosion protection, directly addressing regulatory and environmental pressures facing the coatings industry. Traditional chromate conversion coatings, long the gold standard for aluminum protection, are increasingly banned due to the carcinogenicity of hexavalent chromium. Zinc phosphate and zinc molybdate pigments, while less toxic, require high loadings (20–30 wt%) to achieve modest performance gains, increasing coating density, raw material costs, and VOC emissions due to higher solids content. In contrast, Ce-PA is derived from phytic acid, a renewable, plant-extracted organophosphate abundant in cereal grains and oilseed processing waste. Its synthesis requires only a simple precipitation step with cerium nitrate, avoiding high-energy processes or hazardous solvents. The 4 wt% loading level represents a step-change in pigment efficiency, reducing the mass of functional additive by 5–7× relative to conventional systems. From a life-cycle perspective, this translates into lower embodied energy, reduced transportation emissions, and decreased end-of-life waste volume. Furthermore, the absence of heavy metals such as chromium, lead, or cadmium ensures compliance with global regulations including REACH, RoHS, and China's GB standards. Looking forward, the Ce-PA concept is highly extensible. Substituting cerium with lanthanum or neodymium could tailor inhibition for magnesium or steel alloys. Functionalizing the phytate ligand with silane groups could enhance interfacial bonding with the epoxy matrix, further suppressing agglomeration. Scaling production will require transitioning from batch precipitation to continuous flow synthesis, but the simplicity of the chemistry suggests strong manufacturability. Ultimately, the success of Ce-PA lies not just in its 98.7% inhibition efficiency or its 50-day impedance stability, but in its embodiment of a new design philosophy: leveraging bio-derived, earth-abundant chemistries to deliver performance that rivals or exceeds legacy toxic systems. For the aerospace and marine sectors — where aluminum alloys dominate and corrosion costs are measured in billions—Ce-PA offers a credible, drop-in pathway to greener, longer-lasting protection.

4.5 Remaining Scientific Gaps, Accelerated Aging Validation, and the Pathway to Industrial Adoption

While the results are compelling, several critical questions must be resolved before Ce-PA can transition from laboratory validation to commercial deployment. First, the long-term stability of the $Al_n(PA)_3/Ce(OH)_4$ layer under cyclic wet–dry conditions or in the presence of aggressive anionic contaminants (e.g., sulfate, thiosulfate) remains untested. Pitting corrosion in aluminum alloys is often initiated by aggressive anions that displace passive layer components; future work should evaluate whether the phytate-based film can resist such displacement. Second, the mechanical robustness of the coating under thermal cycling must be verified. Aluminum aircraft skins experience temperatures ranging from −50 °C to +80 °C, inducing differential thermal contraction/expansion between the epoxy, pigment, and substrate. While 4 wt% loading preserves flexibility in standard impact and bend tests, real-world service involves complex multiaxial stresses that could propagate micro-cracks and trigger localized inhibitor release. Accelerated aging protocols combining UV exposure, thermal shock, and salt fog (ASTM D5894) should be employed to simulate multi-year field exposure. Third, the interaction between Ce-PA and common epoxy additives — such as flow modifiers, UV stabilizers, and cosolvents—requires systematic screening to avoid unintended antagonism. Finally, economic feasibility must be rigorously assessed. Although phytic acid is bio-derived, its current market price is higher than that of commodity phosphates; however, this cost differential is offset by the dramatically lower required loading. A detailed techno-economic analysis comparing Ce-PA against zinc phosphate and chromate primers across a 10-year lifecycle would solidify its value proposition. Pilot-scale trials on actual aircraft or ship components, coupled with non-destructive monitoring of impedance degradation, represent the final validation milestone. Should these

tests confirm laboratory-scale performance, Ce-PA stands poised to become a cornerstone of next-generation, sustainable anti-corrosion coatings.

5 Conclusions

Bio-derived anti-corrosion pigment nano-cerium phytate was successfully synthesized through a single-step protocol and subsequently dispersed within epoxy resin matrix to manufacture protective coatings.

(1) Ce-PA has an average particle size of 185 nm, exhibiting good dispersibility and thermal stability. It disperses uniformly in the epoxy resin. However, excessive loading (8%, 10%) leads to agglomeration within the coating, compromising its corrosion resistance.

(2) When aluminum alloy is immersed in nano-Ce-PA leachate, a protective film forms on its surface, effectively shielding it from corrosion, achieving a protection efficiency of up to 98.7%.

(3) The addition of nano-Ce-PA effectively enhances the corrosion resistance of epoxy coatings. The coating formulation containing 4% Ce-PA (EP-4) demonstrates optimal performance characteristics. Following 50-day immersion in 3.5 wt% NaCl solution, its coating resistance is maintained at 5.9×10^{8} Ω·cm². Even for defective coatings, the resistance remains at 7.5×106Ω · cm2after 14 days of immersion.

(4) Ce-PA hydrolyzes in water to generate Ce^{4+} and PA^{n-}. Ce^{4+} reacts with OH^- to form $Ce(OH)_4$, while PA^{n-} chelates with Al^{3+} to form $Al_n(PA)_3$. The dense protective film composed of $Al_n(PA)_3$ and $Ce(OH)_4$ effectively protects the aluminum alloy, thereby improving the corrosion resistance of the epoxy coating.

References

[1] Deng J H, Chen D Y, Zhang B, et al. Application of PCA-ANN on prediction of corrosion data for aluminum alloy of typical aviation material. Environmental Technology, 2023, 41(5): 97-103.
[2] Yang L Y. Research on corrosion resistance of laser coated coating of aviation aluminum alloy [D]. Shanghai: Donghua University, 2022.
[3] Zhang Q. Current status and prospects of heat-resistant aluminum alloys. Nonferrous Metals Processing, 2021, 50(1): 1-4.
[4] Cao L, Chen B, Jia Z D, et al. Research progress and aerospace applications of aluminum matrix composites. Foundry Technology, 2023, 44(8): 685-705.
[5] Wu Y Z, Su Y P, Kong D C. Application and development of aluminum alloy pipe in ship. Marine Equipment, 2020(5): 21-22.
[6] Liu Y, Lin Z F, Zhao R, et al. Feasibility study on application of aluminum alloy cable in ship industry. Guangdong Shipbuilding, 2019, 38(2): 86-89.
[7] Yeganeh M, Omidi M, Rabizadeh T. Anti-corrosion behavior of epoxy composite coatings containing molybdate-loaded mesoporous silica. Progress in Organic Coatings, 2019, 126: 18-27.
[8] Suleiman R K, Adesina A Y, Kumar A M, et al. Anticorrosion properties of a novel hybrid sol-gel coating on aluminum 3003 alloy. Polymers, 2022, 14(9): 1798.
[9] Guo F, Cao Y Z, Wang K J, et al. Effect of the anodizing temperature on microstructure and tribological properties of 6061 aluminum alloy anodic oxide films. Coatings, 2022, 12(3): 314.
[10] Huang X Q, Yang J J, Chen C J, et al. Research progress on functional epoxy-based anti-corrosion coatings. Fine Chemicals, 2023, 40(8): 1625-1635, 1666.
[11] Ju J J, Wang Y, Yu M H, et al. Preparation and study of modified phytic acid/epoxy resin anti-corrosion coating. Colloid and Polymer Science, 2024, 302(1): 117-127.
[12] Liu Z S, Liu C, Chi L, et al. Preparation and corrosion resistance of phytic acid conversion coating on aluminum alloys. Plating and Finishing, 2023, 45(11): 54-59.
[13] Shi H W, Han E H, Liu F C, et al. Protection of 2024-T3 aluminium alloy by corrosion resistant phytic acid conversion coating. Applied Surface Science, 2013, 280: 325-331.
[14] Yang H, Xu N, Liu X Y, et al. The dual pretreatment of phytate-molybdate for corrosion resistance of carbon steel in simulated concrete pore solution. Journal of Building Engineering, 2023, 78: 107643.

[15] Fahrenholtz W G, O'Keeffe M J, Zhou H F, et al. Characterization of cerium-based conversion coatings for corrosion protection of aluminum alloys. Surface & Coatings Technology, 2002, 155(2): 208-213.
[16] Machkova M, Matter E A, Kozhukharov S, et al. Effect of the anionic part of various Ce(III) salts on the corrosion inhibition efficiency of AA2024 aluminium alloy. Corrosion Science, 2013, 69: 396-405.
[17] Zhang W, Li J Q, Wu Y S, et al. Corrosion resistance of conversion film formed on aluminium alloy using cerium salt surface treatment. Surface Engineering, 2002, 18(3): 224-227.
[18] Bethencourt M, Botana F J, Cano M J, et al. Protection by thermal and chemical activation with cerium salts of the alloy AA2017 in aqueous solutions of NaCl. Metallurgical and Materials Transactions, 2012, 43(1): 182-194.
[19] Ren S C, Meng F D, Li X M, et al. A self-healing epoxy composite coating based on pH-responsive PCN-222 smart containers for long-term anticorrosion of aluminum alloy. Corrosion Science, 2023, 221: 111318.
[20] Li Y, Liu X H, Qian Y, et al. Preparation and property of functionalized bacterial cellulose composite. New Chemical Materials, 2017, 45(9): 247-249.
[21] Lin D Y. Effects of phytic acid sealing on corrosion resistance of electroless Ni-P plating layer on aluminum cable steel reinforced. Materials Protection, 2016, 49(12): 50-53.
[22] Yang G C, Zhang Q H. Preparation of bio-based flame-retardant kraft paper by chelating self-assembly and its flame-retardant mechanism. Polymer Materials Science & Engineering, 2022, 38(10): 46-55.
[23] Zhong X M, Zhou W, Wang X, et al. Infrared spectroscopic and thermal analysis of cerium acetate crystal. Journal of Nanchang Hangkong University (Natural Sciences), 2005(3): 50-52.
[24] Chen Y N, Ren B H, Gao S Y, et al. The sandwich-like structures of polydopamine and 8-hydroxyquinoline coated graphene oxide for excellent corrosion resistance of epoxy coatings. Journal of Colloid and Interface Science, 2020, 565: 436-448.
[25] Xue D, Meng Q B, Lu Y X, et al. Achieving high performance anticorrosive coating via in situ polymerization of polyurethane and poly(propylene oxide) grafted graphene oxide composites. Corrosion Science, 2020, 176: 109055.
[26] Liu X W, Xiong J P, Lyu Y W, et al. Study on corrosion electrochemical behavior of several different coating systems by EIS. Progress in Organic Coatings, 2009, 64(4): 497-503.
[27] Li X W, Du S M, Ma C H, et al. Nano-SiO_2 based anti-corrosion superhydrophobic coating on Al alloy with mechanical stability, anti-pollution and self-cleaning properties. Ceramics International, 2024, 50(6): 9469-9478.
[28] Brug G J, Van Den Eeden A L G, Sluyters-Rehbach M, et al. The analysis of electrode impedances complicated by the presence of a constant phase element. Journal of Electroanalytical Chemistry and Interfacial Electrochemistry, 1984, 176(1/2): 275-295.
[29] Cheng L, Wu H, Li J, et al. Polydopamine modified ultrathin hydroxyapatite nanosheets for anti-corrosion reinforcement in polymeric coatings. Corrosion Science, 2021, 178: 109064.
[30] Wang P, Cai D Y. Study of the protection of aluminum alloy surfaces by a graphene-modified fluorocarbon anticorrosive coating. International Journal of Photoenergy, 2020, 2020: 1-8.
[31] Hao Y S, Liu F C, Han E H, et al. The mechanism of inhibition by zinc phosphate in an epoxy coating. Corrosion Science, 2013, 69: 77-86.
[32] Hao Y S, Liu F C, Han E H. Inhibitive behavior and mechanism of a ferrite inhibition pigment in epoxy paints. Journal of the Electrochemical Society, 2012, 159(9): C403-C410.
[33] Chen J F, Zhang Y, Wang Y N, et al. Internal electric field promoted NCDs/BiOBr/AgBr Z-scheme heterojunction with rich oxygen vacancies for efficient photocatalytic degradation of tetracycline and reduction of Cr(VI). Journal of Environmental Chemical Engineering, 2024, 12(3): 112476.
[34] Bano K, Kaushal S, Kumar A, et al. Sunlight-driven photocatalytic degradation of 4-nitrophenol and adsorptive removal of Mn(II) ions from industrial wastewater by biogenic synthesized CuO/SnO_2 heterojunction. Materials Today Chemistry, 2022, 26: 101193.
[35] Zhong X, Ling Q, Wang S, et al. Visible-light-driven 2D/2D bismuth oxyhalides/covalent organic framework heterojunctions for synchronous photocatalytic U(VI) reduction and bisphenol A degradation. Journal of Environmental Chemical Engineering, 2022, 10(4): 108097.
[36] Jasim N A, Ammar S H, Ebrahim S E. Assembling $ZnMnFe_2O_4$@Ag-$AgVO_3$ nanostructure heterojunctions for photocatalytically degrading RhB and Pseudomonas aeruginosa bacteria under visible irradiation. Journal of Photochemistry and Photobiology A: Chemistry, 2024, 449: 115380.
[37] Kokilavani S, Syed A, Kumar B H, et al. Facile synthesis of MgS/Ag_2MoO_4 nanohybrid heterojunction: Outstanding visible light harvesting for boosted photocatalytic degradation of MB and its anti-microbial

applications. Colloids and Surfaces A: Physicochemical and Engineering Aspects, 2021, 627: 127097.

[38] Zhong S Q, Wang Y B, Chen Y, et al. Improved piezo-photocatalysis for aquatic multi-pollutant removal via $BiOBr/BaTiO_3$ heterojunction construction. Chemical Engineering Journal, 2024, 488: 151002.

[39] Tran V T, Chen D H. $Ag_2O@BiFeO_3$ heterostructure composite coupling built-in electric field with piezopotential for enhanced photocatalytic pollutant degradation and photoelectrochemical water splitting. Applied Surface Science, 2023, 625: 157175.

[40] Zhou X Y, Liu Y Y, Miao Y Q, et al. Coupled radical and non-radical activation of peroxymonosulfate by the piezo-photocatalytic effect of a-$SnWO_4$/ZnO heterojunction to boost the degradation and detoxification of carbamazepine. Separation and Purification Technology, 2023, 323: 124410.

[41] Yu S Y, Xie Z H, Wu X, et al. Review of advanced oxidation processes for treating hospital sewage to achieve decontamination and disinfection. Chinese Chemical Letters, 2024, 35(1): 108714.

[42] Jing Q F, Liu Z Y, Cheng X, et al. Boosting piezo-photocatalytic activity of $BiVO_4/BiFeO_3$ heterojunctions through built-in polarization field tailoring carrier transfer performances. Chemical Engineering Journal, 2023, 464: 142617.